Separation and Purification Technology, Volume 350, December 2024, Article number 127826
DOI: 10.1016/j.seppur.2024.127826

Design of novel Sb_2S_3/Polythiophene heterojunction for efficient adsorption and Methanol Sensing

Nafees Ahmad[1*], Qazi Inamur Rahman[1], Arshad Iqbal[2], Masoom Raza Siddiqui[3], Saikh Mohammad Wabaidur[3], Naseem Ahmad[1], Frederic Coulon[4]

[1]*Department of Chemistry, Integral University, Lucknow, 226026, India*
[2]*Department of Physics, Integral University, Lucknow, 226026, India*
[3]*Chemistry Department, College of Science, King Saud University, Riyadh 11451, Saudi Arabia*
[4]*School of Water Energy and Environment, Cranfield University, Cranfield, MK 43 0AL, UK*

Abstract

Eliminating micropollutants in trace concentrations in water bodies is crucial and challenging due to their persistent and bioactive characteristics. Due to these characteristics, their detection and removal pose a challenge to the conventional removal methods and to the health of the community. To effectively remove the pollutants, it requires the design and development of an efficient technique compared to the conventional techniques. The design of highly efficient methanol sensor and the adsorption of micropollutants by a heterojunction involving Sb_2S_3 and polythiophene (PTh) looks promising. The adsorption study was targeted on RhB dye whereas methanol was targeted to sensing application. Sb_2S_3 nanoparticles was synthesized by hydrothermal methods and incorporated into thiophene solution during chemical oxidative polymerization of thiophene. The heterojunction was applied to remove RhB dye through the adsorption process. Freundlich isotherm model and Langmuir isotherm model were used to study the adsorption of RhB. The higher adsorption capacity was found in case of Sb_2S_3/PTh is 99.8 mg g^{-1}, and the rate constant (K_2) was found to be 0.0206 min^{-1}. The catalysts follows the pseudo-first and second order kinetics in the removal of RhB dye. The rate constant for adsorption k_1 is 0.1347min^{-1} and the rate constant for diffusion is 0.297 min^{-1}. Moreover, the PTh/Sb_2S_3 shows an effective methanol sensing up to 0.7mM and the current response at 0.6756V of the oxidation peaks shows the presence of methanol.

Keywords*:* Sensing, Thermodynamics, Kinetics, Adsorption, heterojunction, methanol sensor

Graphical Abstract

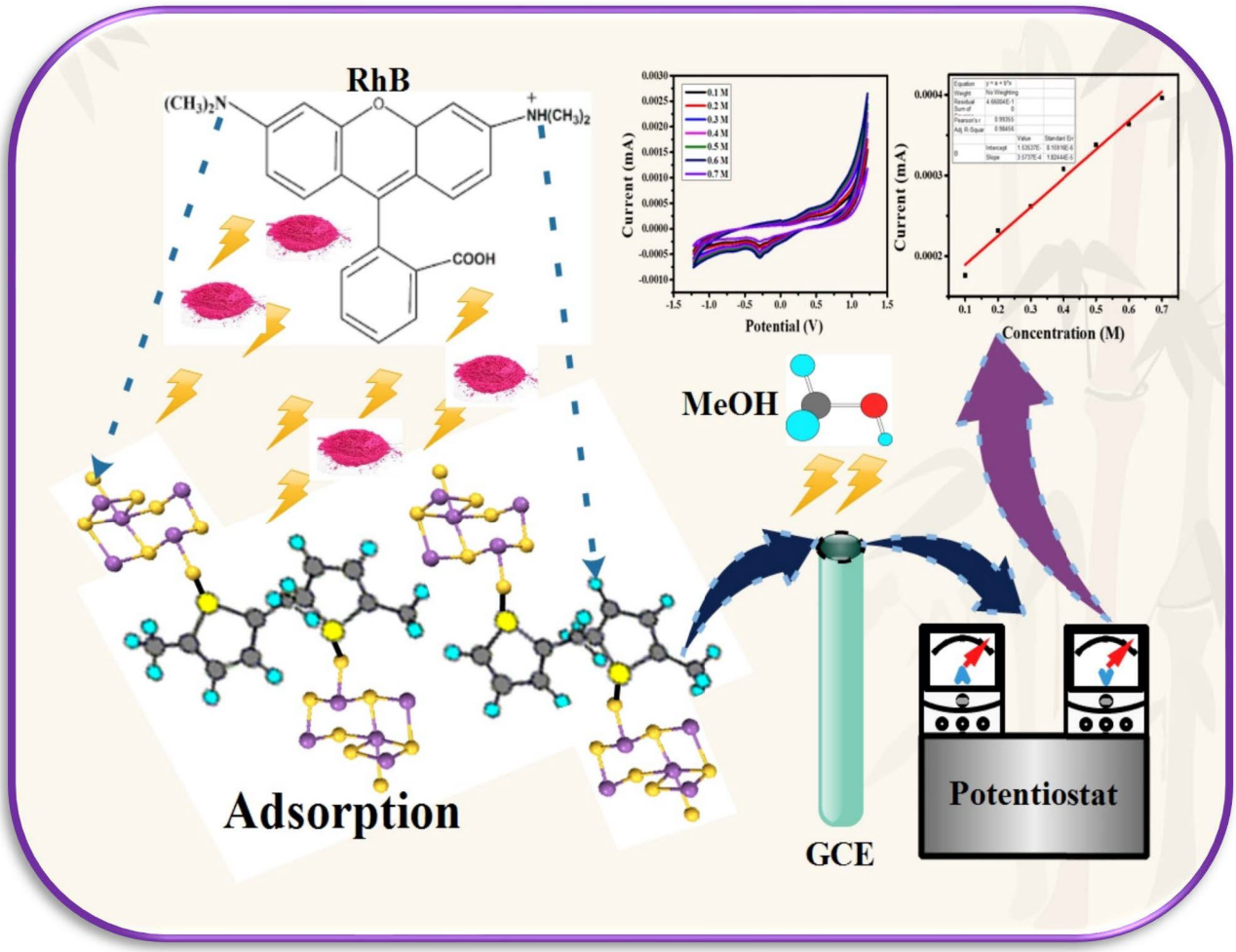

Highlights

- Design of a novel dual-function PTh/Sb_2S_3 as a methanol sensor and adsorption property.
- Langmuir model, the equilibrium data exhibits superior fitting as compared to the Freundlich model with (R_L^2 =0.97).
- Lower concentration (0.1 mM) of methanol are detected using cyclic voltammetry technique by PTh/Sb_2S_3.
- The correlation coefficient R_d^2 = 0.99 for diffusion and R_a^2 = 0.76 for adsorption indicate the catalysts follows both pseudo first and second order kinetics.

1. INTRODUCTION

The rise of toxic micropollutants in water bodies around the world has emerged as a pressing concern posing significant threats to human health and the environment. This increase is largely attributed to industrial processes, including manufacturing, chemical production, and fuel production, resulting in the increased presence, accumulation, and concentrations of hazardous micropollutants in the environment (Bolisetty et al. 2019, Kümmerer et al. 2019, Ahmad et al. 2021). Of specific concern are textile dyes, due to their complex chemical compositions, stability, and resistance to biodegradation. (Routoula et al. 2020, Katheresan et al. 2018). Their presence in water bodies not only diminishes water quality by reducing dissolved oxygen levels, thus impairing vital processes like photosynthesis and respiration, but also interferes with light penetration through sunlight reflection, disrupting water ecosystems (Al-Tohamy et al. 2022). Conventional techniques for micropollutant remediation, such as adsorption, ion exchange, and advanced oxidation processes, have been employed to varying degrees of success. Among these methods, adsorption stands out for its simplicity, efficiency, and applicability across a wide range of pollutant concentrations without generating harmful byproducts. However, there remains a pressing need for innovative solutions to enhance the effectiveness and sustainability of micropollutant removal from water bodies. Therefore, the adsorption process featuring cost effectiveness, less energy consumption and reusability of the catalysts are an effective approach in the removal of micropollutants (Ahmad et al. 2023, Nure et al.2023).

In this context, the development of novel catalysts with dual functionality such as the simultaneous degradation of micropollutants and sensing of organic solvents like methanol through electrochemical technique holds immense promise. As this dual functionality approach combines the benefits of the adsorption techniques as well as the sensing technology could be a viable solution for the environmental remediation. By using a single catalyst, detection as well as removal of pollutants can be done. (Liang et al. 2023, Saleh et al. 2019, Molla et al. 2019). Methanol is commonly used solvent in various industrial processes for the chemical and fuel production. Monitoring methanol levels in water bodies near industrial facilities helps ensure compliance with regulations and prevents accidental releases or contamination. Detecting methanol in water bodies allows for early identification of contamination events, enabling timely remediation efforts to protect ecosystems and public health. So methanol sensing provides a means to assess water quality and mitigate potential health risks associated with consumption or exposure.

Such catalysts could offer a multifaceted approach to water treatment, addressing both chemical contamination and the real-time monitoring of solvent concentrations in aquatic environments. By integrating adsorption and sensing capabilities into a single catalyst, it allows optimizing resource utilization, streamline water treatment processes, and mitigate environmental risks associated with micropollutant exposure. (Luo et al. 2014). So far, a number of adsorbents have being utilized for the removal of dyes and other toxic micropollutants such as nanoparticles, nanocomposites, polymer, zeolites, metal organic frameworks (MOFs) and covalent organic frameworks (COFs) and carbon rich material such as graphene, single walled carbon nanotubes (SWCNT) and multiwalled carbon nanotubes (MWCNT) (Bano et al. 2019, Ahmad et al. 2017, Uddin et al. 2021, Zhang et al. 2021, Iqbal et al. 2023). Moreover, several biogenic catalysts extracted from leafs of several trees are also quite efficient in the adsorption of micropollutants (Iqbal et al. 2021).

Our study focuses on investigating the potential of a novel catalyst, comprising polythiophene (PTh) and antimony trisulfide (Sb_2S_3), for the dual purpose of micropollutant degradation and methanol sensing. The electrochemical property, redox property and higher surface area of PTh and Sb_2S_3 makes them for suitable catalyst for sensing of methanol and removal of RhB dye (Ayappan et al. 2020, Xiao et al. 2022, Karimi-Shamsabadi et al. 2021). By taking advantage of the unique properties of PTh as a conducting polymer and Sb_2S_3 as a robust catalyst, our study aims to explore the synergistic interactions that enhance surface area, redox activity, and adsorption capacity for waterborne micropollutants and solvent contamination.

2. EXPERIMENTAL SECTION

2.1 Dual function catalyst synthesis

For the synthesis of Sb_2S_3, antimony chloride ($SbCl_3$ prepared in HCl) 25mL, was dissolved in 1mmol $Na_2S.9H_2O$ (25mL) and stirred for 30 min. The solution was transferred to a Teflon lined hydrothermal autoclave and maintained at 120°C for 12 hrs. The precipitate was then filtered, washed with distilled water and dried at 60°C for 12 hrs (Wang et al. 2016). For the synthesis of PTh/Sb_2S_3, the pre-synthesized Sb_2S_3 was incorporated during the polymerization of thiophene. For the chemical oxidation polymerization of PTh, 1 mL of thiophene was added to 30 mL of $CHCl_3$. Then 4.5 g of $FeCl_3$ solution prepared in $CHCl_3$ was added and the mixture was stirred for

24h. The precipitate was then centrifuged and dried for 60°C for 4 hrs (Faisal et al. 2018). Fig.1 shows the outline for the synthesis of PTh/Sb_2S_3 nanocomposite.

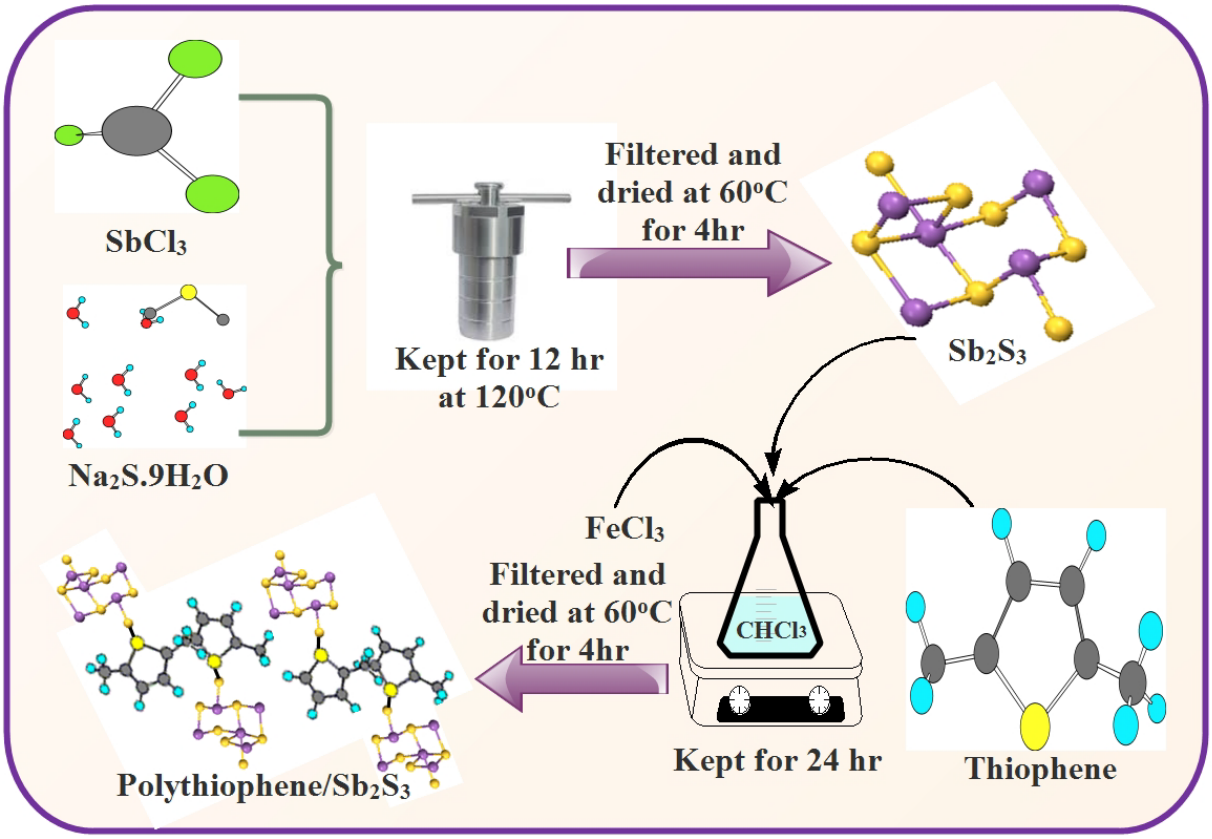

Fig.1 Reaction scheme for the synthesis of PTh/Sb_2S_3 nanocomposite

2.3 Adsorption experiments

The adsorption capabilities of PTh, Sb_2S_3 and PTh/Sb_2S_3 were evaluated against RhB dye using a photochemical reactor (Ahmad et al. 2023). In this study, 100 mg of each catalyst was mixed with 100 ml aqueous solution of RhB (20ppm) in the reactor which was continuously stirred for 30 mins. The reactor containing the photocatalyst-dye solution mixture was sealed, and room temperature was maintained to allow for adsorption equilibrium in 30 mins. Subsequently, aliquots were periodically withdrawn from the reactor to measure absorbance at 554 nm wavelength, indicating the extent of dye adsorption on the catalyst surface. The amount of RhB dye adsorbed on the surface of PTh/Sb_2S_3 was calculated by the following equation (1):

$$\text{Amount of dye adsorbed} = \frac{C0-Ce}{M} * V \qquad (1)$$

where C_0 and C_e represents the initial and equilibrium concentration in ppm, V is the volume of the RhB solution taken and M is the mass of the catalyst in (mg). The percentage adsorption efficiency of PTh, Sb_2S_3 and PTh/Sb_2S_3 against RhB were calculated by below equation (2)

$$\text{Adsorption efficiency (\%)} = \frac{C0-Ct}{C0} * 100\% \quad (2)$$

On the basis of the results obtained from equation (1) and (2), the thermodynamics of adsorption using Freundlich and Langmuir isotherm and the kinetics of adsorption using pseudo first and second order were studied. All the experiments performed were replicated twice.

2.4. Catalyst characterizations

The morphology, elemental composition and the particle size of the catalysts were analyzed transmission electron microscopy (TEM) and scanning electron microscopy (SEM) coupled with energy-dispersive X-ray spectroscopy (EDX) (JSM 6510 LV JEOL, Japan). The crystalline nature of the photocatalyst were determined using X-ray diffractometer (Model: MiniFlex600/600-C). Functinal group analysis was done by using OPUS version (Alpha II, 210966). The absorbance of 5ml of RhB solution in concentration ranges 2-20 ppm against the photocatalysts in the aqueous solution was checked using UV-visible spectrophotometer (Agilent Technologies) at 554nm wavelength. In addition BET analysis, was carried out by using by Quantachrome Instruments version 5.21 to calculate the surface area and pore volume and pore size.

3. RESULTS AND DISCUSSION

3.1 Structural, functional groups and Microscopic studies

To assess the purity and crystalline phase of the synthesized samples, X-ray diffraction (XRD) analysis was conducted over a 2θ range of 10° to 80°. In Fig. 2a, the XRD patterns of Sb_2S_3, PTh and PTh/Sb_2S_3 are presented. The obtained results reveal distinct and well-defined diffraction peaks, indicative of a high level of crystallization in prepared samples. Notably, there is an absence of diffraction peaks corresponding to impurities in the XRD patterns of Sb_2S_3 nanoparticles, affirming the high purity of Sb_2S_3. The XRD spectra for all samples consistently match the orthorhombic pure phase of crystalline stibnite-Sb_2S_3, with a Pbnm (62) space group symmetry. The characteristic peaks at 2θ = 28.0, 28.2, 31.1, and 31.3° align with the (2 3 0), (2 1 1), (3 0 1),

and (2 4 0) planes. The results revealed a partially crystalline broad peak centered on 2θ value of 22.2°. The presence of a robust diffraction peak at approximately 2θ = 22.2° is attributed to the amorphously arranged PTh main chain, indicative of chain-to-chain stacking distances (Hadia et al. 2019, Kalangestani et al. 2020). A small peak related to PTh was clearly seen in the XRD pattern of PTh/Sb_2S_3 sample in Fig.2a. The shifting of Sb_2S_3 peaks in the PTh/Sb_2S_3 spectra is due to the formation of heterojunction. Further Fig. 2b illustrates the Fourier transform infrared spectra of Sb_2S_3, PTh and PTh/Sb_2S_3 providing confirmation of the formation of antimony sulfide bonds. In the Fourier transform infrared (FT-IR) analysis, bonds within the 2500–4000 cm^{-1} range are associated with O–H bond stretching vibrations, indicating the presence of water in the compound (Trivedi et al. 2015). Peaks at 612, 742, and 1639 cm^{-1} are attributed to Sb-S symmetric stretching vibrations. Absorption bands at 1072 and 1124 cm^{-1} are related to C–OH bond or charge delocalization (Dashariya et al. 2018, Subramanian et al. 2010). The peak at 1278 cm^{-1} corresponds to S–C bonding (Hou et al. 2018). An absorption peak at 1383 cm^{-1} is indicative of a metal-sulfide bond (Subramanian et al. 2010), while the peak around 1463 cm^{-1} is assigned to C–H bond flexural vibrations (Tezel et al. 2019). The peak at 1729 cm^{-1} is attributed to C=O stretching vibrations (Dashariya et al. 2018). Changes in peak intensity, shape, and position are attributed to the interaction between PTh and Sb_2S_3 nanorods. The spectrum of PTh polythiophene exhibits key features, including the (C-H) stretching vibration band at 2923 cm^{-1}, the (C=C) stretching band spanning 1458-1596 cm^{-1}, the (C-H) in-plane bending band at 1113 cm^{-1}, and the (C-S) bending band at 749 cm^{-1}. The absorption frequencies of the polymer undergo a shift due to increased conjugation, as supported by these results in relation to polymerization (Kalangestani et al. 2020). The Morphological properties of the photocatalyst are presented in Fig. 2 (c,d). The nanopetals of the Sb_2S_3 are clearly seen in Fig. 2c and the Sb_2S_3 nanopetals are agglomerated to the porous surface of PTh as seen in Fig. 2d. The elemental composition of PTh/Sb_2S_3 are shown in Fig. 2 (e, f) which shows the formation of the photocatalyst. TEM was employed for an in-depth investigation of the morphology and crystal structures. Fig.2g showcase a segment of the as-prepared Sb_2S_3 and PTh/Sb_2S_3 exhibiting diameters within the range of 100–180 nm and lengths spanning 3–5μm. The Sb_2S_3 nanoparticles are agglomerated on the surface of PTh sheets. Fig.2g provides a clear indication of the successful incorporation of Sb_2S_3 nanoparticles within the PTh matrix. Furthermore, the lattice fringes, characterized by a d-spacing of 0.38 nm, align well with the (001) planes of orthorhombic Sb_2S_3 (Xiao et al. 2013). This evidence leads to the conclusion

that the Sb_2S_3 possess crystalline properties, with a preferential growth direction along (001). Fig.2h displays the average particles size of the PTh/Sb_2S_3 composite. The average particle size is found to be 19.13nm.

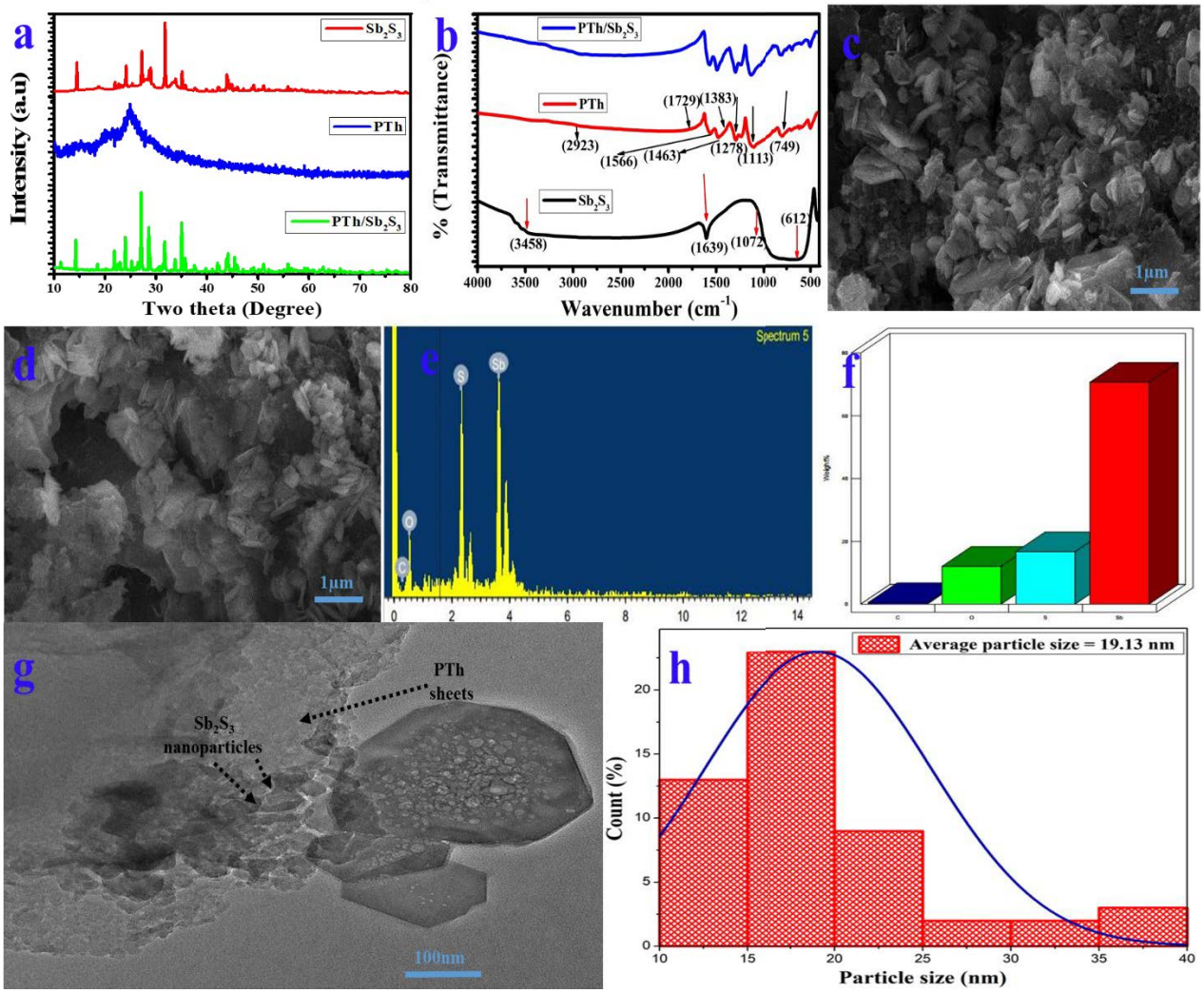

Fig.2. (a) XRD spectra and (b) FTIR spectra of Sb_2S_3, PTh and PTh/Sb_2S_3 (c) SEM image of Sb_2S_3(d) SEM image of Sb_2S_3/PTh, (e, f) EDX image for the elemental composition, (g)TEM image of Sb_2S_3 and (h) Average particles size of nanocomposite

3.2. BET and XPS Analysis

BET analysis was carried out to determine the surface area, pore size and pore volume of the photocatalyst as shown in Fig. 3. The surface area, pore size and pore volume of the Sb_2S_3 are 67m^2/g, 11.2cc/g and 0.0457cc/g and for the PTh/Sb_2S_3 the surface area, pore size and pore volume

are 74m^2/g, 9.24cc/g and 0.0346cc/g respectively. The BET isotherm in Fig. 3 (a, b) shows the formation of type II isotherm in which the region (0.2-0.8) of P/P_0 seems to be the flatter and is due to the formation of monolayer formation. In Fig. 3(c, d) the average pore size calculated form the spectra is found to be 4nm and 8nm which shows that the nature of the photocatalysts are mesoporous. Further it can be conclude that the surface are of Sb_2S_3/PTh is higher that Sb_2S_3 because of the doping that eventually helps in the adsorption of MPs on its surface.

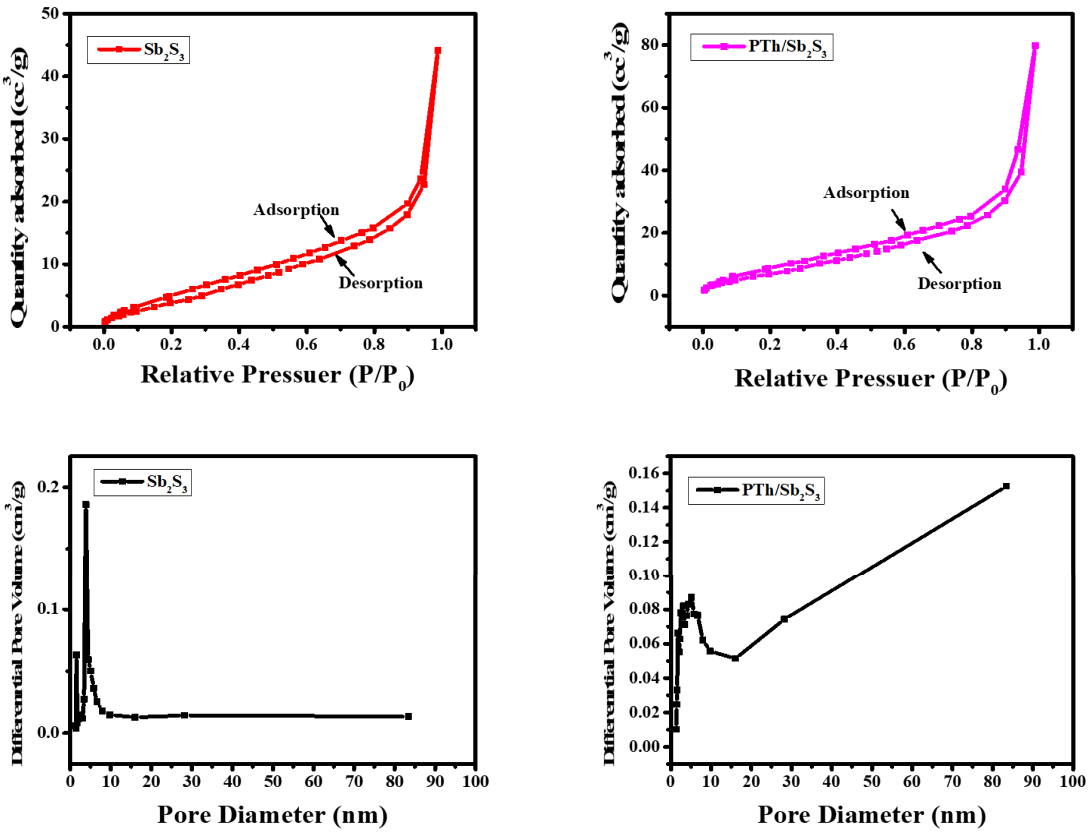

Fig.3. BET isotherm and pore size distribution of Sb_2S_3 and PTh/Sb_2S_3

Further, the XPS analysis was performed to characterize the chemical states, the surface elemental composition of the Sb_2S_3 and Sb_2S_3/PTh catalysts and to identify any impurities present. From the Fig.4 the peaks of Sb, S and C are identified as shown in the survey scan of PTh/Sb_2S_3. The binding energy peaks of (Sb 3d 5/2) (Sb 3d 3/2) are located around 532 eV and 537eV respectively and the (S 2p1/2) are located around 154eV and 161eV and the peak around 288eV of C 1s spectrum confirmed the sp^2 hybridized carbon in the PTh.

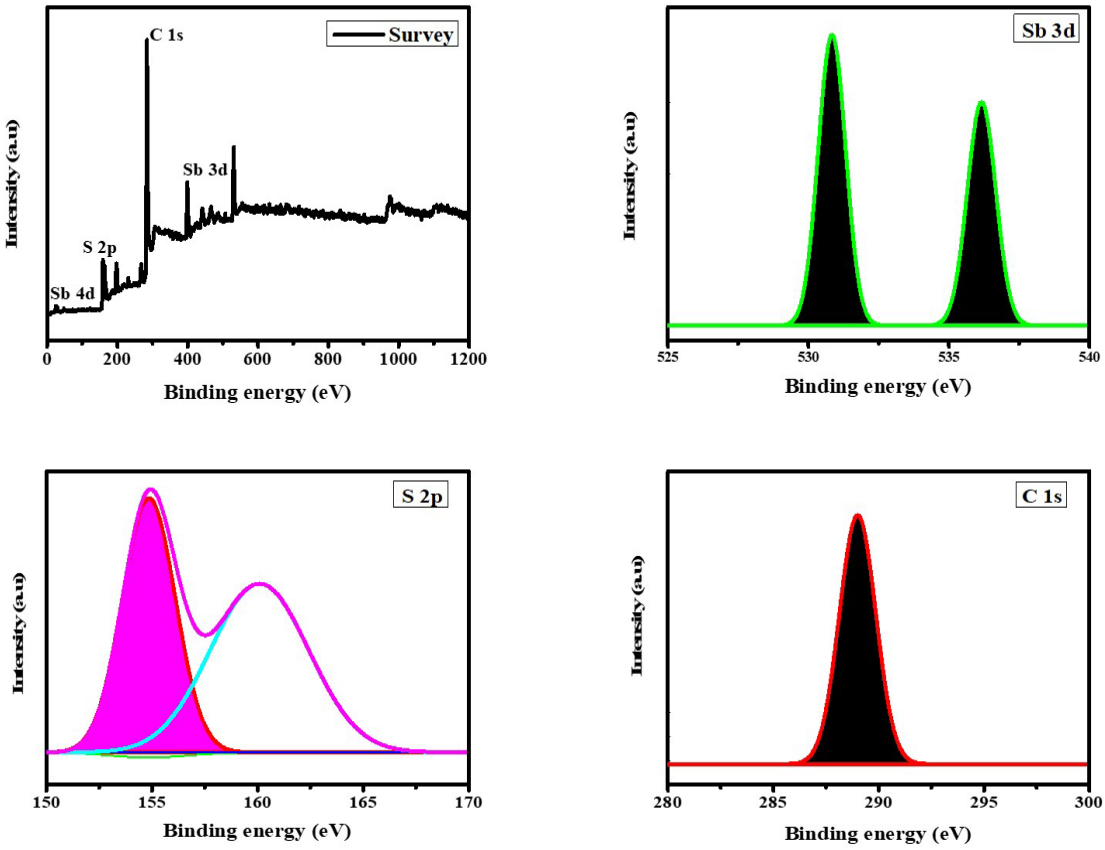

Fig.4. XPS survey of the elemental state of Sb_2S_3/PTh nanocomposite

3.4. Electrochemical Sensing of methanol Using Cyclic Voltammetry

Methanol is a highly volatile and colorless and its exposure in minute concentration in the environment caused poising, multi organ failure and even caused to death. Methanol poisoning leads to serious issues such as headache, allergy, fatigue, and narcosis in human beings (Bano et al. 2019). The concentration of methanol for the human intake is less than 5mg/dl is considered to be safe (Hassanian et al. 2018). Hence, there is a necessity for a straightforward and reliable approach to measure minute amounts of methanol found in human consumption. In this regards, sensing of methanol by electrochemical studies could be a viable technique and diagnose the amount of methanol present in any sample. In the present study, cyclic voltammetry (CV) technique has been used for the determination of methanol using glassy carbon electrode (GCE). CV has been proved to be a reliable technique for sensing of toxic solvents using nanomaterials and conducting polymers (Wang et al. 2018). In this technique, the reduction and the oxidation of the analyte under a given potential and the change in the current is recorded. For the detection of

methanol, oxidation peaks has been considered as the standards. In this study, the electrocatalytic property of the Sb_2S_3 and Sb_2S_3/PTh against methanol were examined in 0.1 mM DMSO at room temperature using CV. The assembly for the cyclic voltammetry using working electrode (GCE) for methanol detection are presented in Fig.S1 (Supplementary information).

Electrochemical activity by CV of bare GCE electrode, and modified GCE electrode with Sb_2S_3 and Sb_2S_3/PTh were performed. For the modification of electrode nafion binder were used for the coating of catalyst on the surface of GCE. From Fig. 5a the CV curve of GCE modified Sb_2S_3/PTh GCE with and without 0.1mM of methanol solution can be clearly observed. The CV response with DMSO is almost negligible however in the presence of 0.1mM methanol, the oxidation peaks can be clearly seen that shows the presence of methanol (Chung et al. 2016). Further, the CV response of Sb_2S_3 and Sb_2S_3/PTh was performed as shown in Fig.5b, in case of Sb_2S_3 less redox response was recorded and in case of Sb_2S_3/PTh higher current response was recorded against 0.1mM which is due to the synergistic behavior of both Sb_2S_3 and PTh which produces more catalytic sites and increases electron transfer. Further, the response of methanol with various concentration ranging from 0.1mM to 0.7mM was recorded by Sb_2S_3 and Sb_2S_3/PTh in which characteristic anodic peaks in Sb_2S_3 was recorded at 0.34V and for PTh/Sb_2S_3 at 0.76 V and cathodic peaks around -0.2 V are observed as shown in Fig. 5 (c, d).

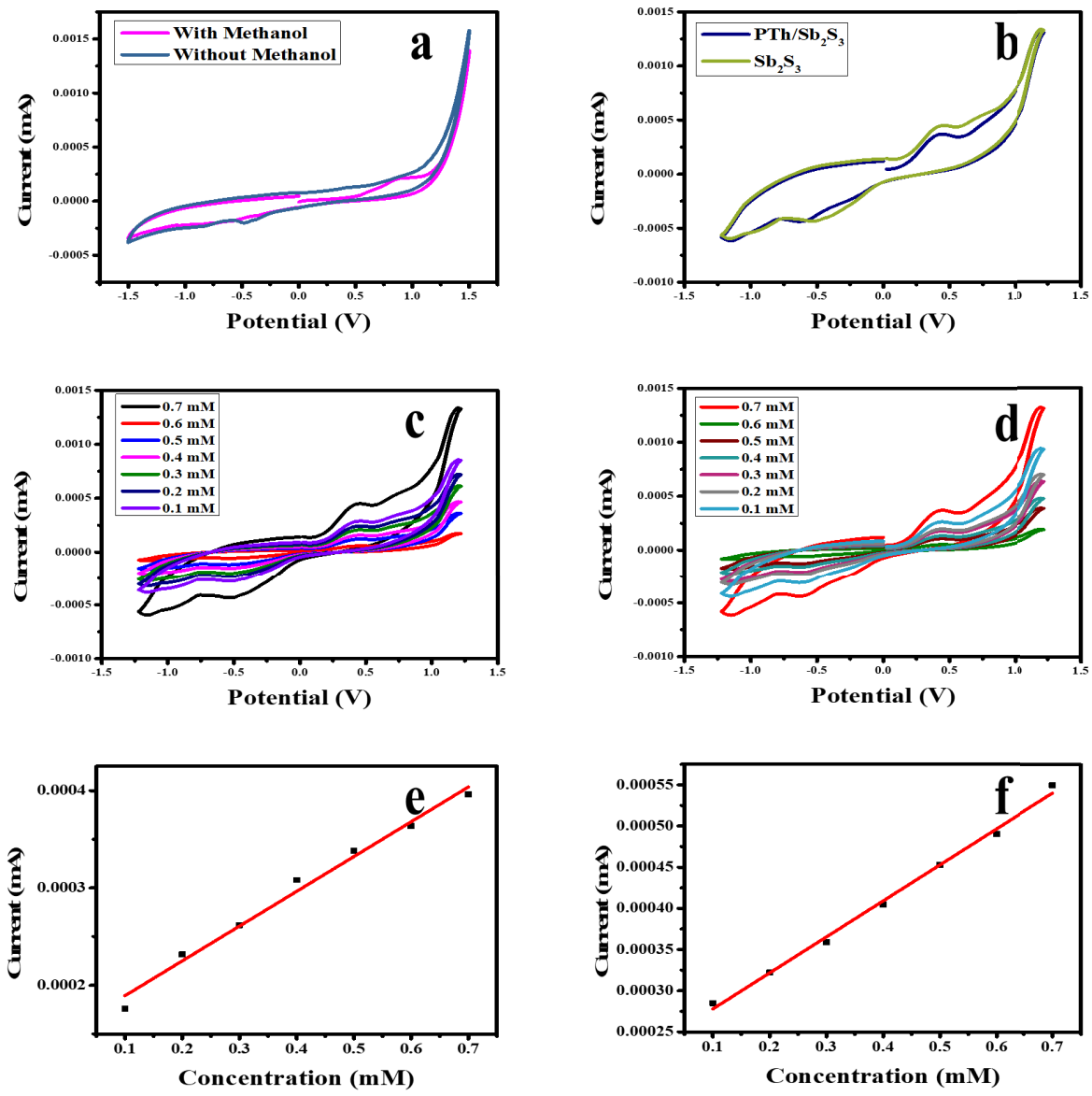

Fig.5. (a) CV curve of bare GCE ear with and without methanol (b) CV response with the modified GCE (c, d) is the CV response of methanol with range of methanol concentration and (e, f) is the calibration curve of Sb_2S_3 and PTh/Sb_2S_3

The variation of anodic peak current with the different concentration of methanol was found to be linear. Form the calibration curve the analytical characteristics of Sb_2S_3 and Sb_2S_3/PTh was calculated as shown in 5 (e, f). From the curve, regression coefficient (r^2 = 0.973), sensitivity

(2.1025 μA mmol L^{-1} cm^{-2}), and limit of detection (LOD: 0.046 mmol L^{-1}) were calculated at the S/N ratio of 3. The LOD was calculated using the following equation (3):

$$LOD = 3\sigma/d \qquad (3)$$

Where σ is the standard deviation and the d is the detection limit of the methanol. From the results it can clear noted that the anodic peak current (oxidation) vary linear with the scan rates. This variation in the peak current is due to the electrode reaction which is the surface controlled electrochemical reaction. Further the rise in the current with varying in the concentration is due to oxidation reaction of methanol. Upon the continuously increasing the concentration of methanol, the surface coverage of the electrode increases that eventually leads to the oxidation of methanol. During the methanol oxidation, the electrons are liberated and leading to increase in the current obtained.

3.5. Evaluation of adsorption thermodynamics and kinetics

The Adsorption kinetics and thermodynamics of Sb_2S_3 and Sb_2S_3/PTh were examined at various concentration ranges from 2ppm to 20 ppm of RhB dye. The adsorption experiment was performed in the acidic medium since the Rh B dye exhibit maximum adsorption in acidic medium (Kusmierek et al. 2023). The mechanism of adsorption of RhB dye at the surface of PTh/Sb_2S_3 nanocomposite is presented in Fig.6.

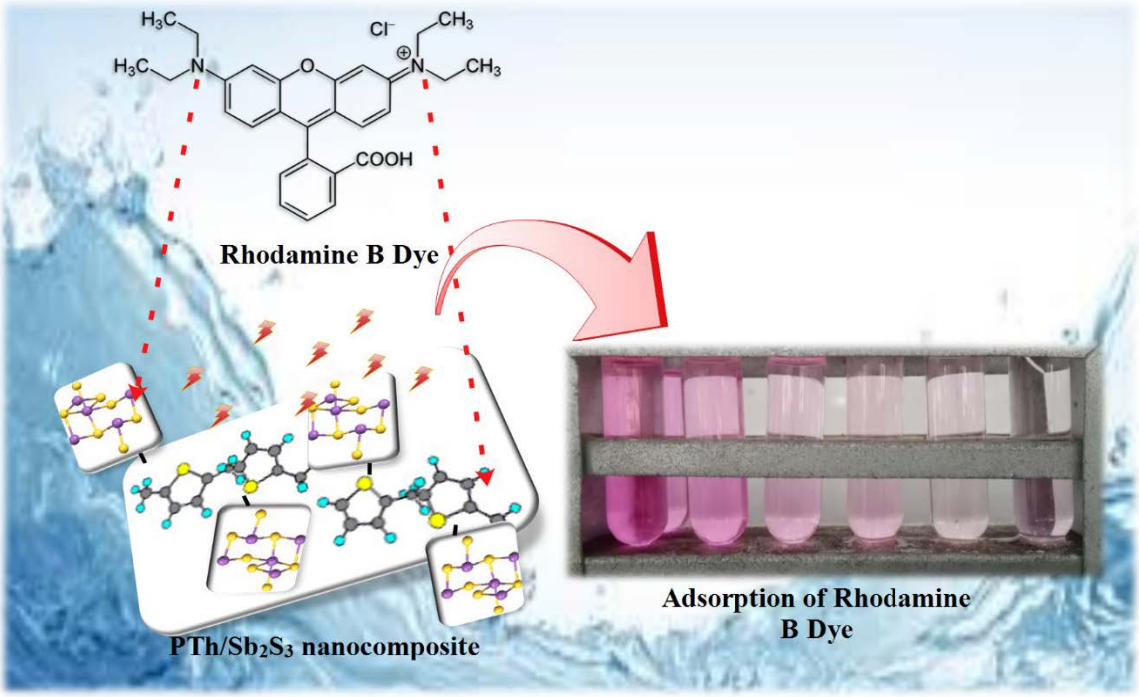

Fig.6. Adsorption mechanism of RhB dye at the surface of PTh/Sb_2S_3 nanocomposite

The adsorption thermodynamics of Sb_2S_3 and Sb_2S_3/PTh were examined by using Freundlich and Langmuir adsorption isotherm. The equations for the Freundlich and Langmuir isotherm are shown below (4, 5):

$$\text{Log } q_e = \log K_f + \frac{1}{n} \log C_e \qquad (4)$$

$$\frac{Ce}{qe} = \frac{Ce}{qe} + \frac{1}{KL\ qm} \qquad (5)$$

In equation (4) K_f represents the Freundlich equilibrium constant, K_L is the Langmuir adsorption, n is a constant of Freundlich adsorption intensity. In equation (5), q_e is the equilibrium adsorption capacity of qm is the maximum adsorption capacity of the catalysts. From the results obtained, the fitting parameters and correlation coefficients of Freundlich and Langmuir adsorption isotherm are presented in Table 1 and the plots of Freundlich and Langmuir adsorption isotherm are presented in Fig. 7 a, b.

Table 1: Parameters for the Langmuir and Freundlich model for the adsorption of RhB dye on the photocatalysts

Langmuir model		
Maximum Adsorption Capacity (q_m (mg g^{-1}))	Adsorption constant (K_L)	Correlation coefficient R_L^2
99.8	0.029	0.97
Freundlich model		
Adsorption constant (K_F)	Adsorption intensity (n)	Correlation coefficient R_F^2
2.21	1.61	0.93

The adsorption of RhB dye onto the Sb_2S_3/PTh surface is characterized by the monolayer adsorption in which the dye molecules are in contact with PTh/Sb_2S_3 surface. The Langmuir model represented the homogenous distribution of adsorbate molecules on the adsorption sites on the adsorption's surface and this leads to monolayer adsorption while on the contrary Freundlich model is known to describe the non-ideal and reversible adsorption, which was not restricted to the formation of monolayer but leads to the multilayer adsorption. Interestingly, both models efficiently demonstrated to analyze the adsorption behavior of adsorbate molecules over the surface. It was interesting to notice that in the preceding research people used to apply both models efficiently and evaluated which one would be the best suited to discuss the adsorption behavior of adsorbate.

In our study, we have efficiently demonstrated Langmuir and Freundlich model to check which model would be best fitted to describe the adsorption of the Dye. Interestingly, it was good to observed that the Langmuir model exhibits better fitting as compared to the Freundlich model which was efficiently confirmed through correlation coefficient (Kumar et al. 2019). In the Langmuir model, the equilibrium data exhibits superior fitting as compared to the Freundlich model. The Langmuir model shows a higher correlation coefficient ($R_L^2 = 0.97$) as compared to Freundlich model ($R_F^2 = 0.93$). A maximum adsorption capacity of the photocatalysts Sb_2S_3, PTh and PTh/Sb_2S_3 is presented in Fig. S2 (Supplementary information). The study further examines into the kinetics of dye removal, employing pseudo first-order and second-order kinetics models. These models are employed to analyze the experimental data and identify the optimal fit for the adsorption of RhB dye on the Sb_2S_3/PTh surface, elucidating the mechanisms involved in the adsorption process. The adsorption process involves the interaction of RhB with the photocatalyst surface, followed by a chemical reaction. The initial diffusion process is governed by a

concentration gradient occurs between the interface and bulk driving the RhB diffusion to the Sb_2S_3/PTh surface. The diffusion process shows relation between the RhB concentration and the adsorption sites of Sb_2S_3/PTh and kinetic rate is established in the diffusion process. Consequently, the diffusion process is studied using the pseudo second order kinetic model to determine the model that best fitted with the experimental data obtained by equations (6, 7) below.

$$\frac{d\theta t}{dt} = k_d^2 (\theta e - \theta t) \quad (6)$$

$$\ln (\theta e - \theta t) = \ln \theta e - K_a t \quad (7)$$

From the equation (6, 7), θ is the coverage fraction adsorbed on the surface of the photocatalyst at time "t" and at the equilibrium "e" respectively. K_a and K_d are the rate constant for adsorption and diffusion. Moreover pseudo first and second order rate expression can be represented as given below in equations (8, 9):

$$\ln (q_e - q_t) = \ln q_e - K_1 t \quad (8)$$

$$\frac{t}{qe} = \frac{1}{K_2\, qe^2} + \frac{1}{qe} \quad (9)$$

Form equations (8, 9) "q_e" (mg g^{-1}) is the amount of RhB adsorbed at equilibrium and "q_t" (mg g^{-1}) is the amount of RhB adsorbed at time "t". K_1 and K_2 (g mg^{-1} min^{-1}) are the adsorption and diffusion rate constant for the pseudo first and second order kinetics. The plots of kinetics of pseudo-first and second order obtained from the experimental date are presented in Fig. 7 c,d. Form the plots, and the higher value "qt" obtained is in case of Sb_2S_3/PTh which shows that higher adsorption of RhB on its surface.

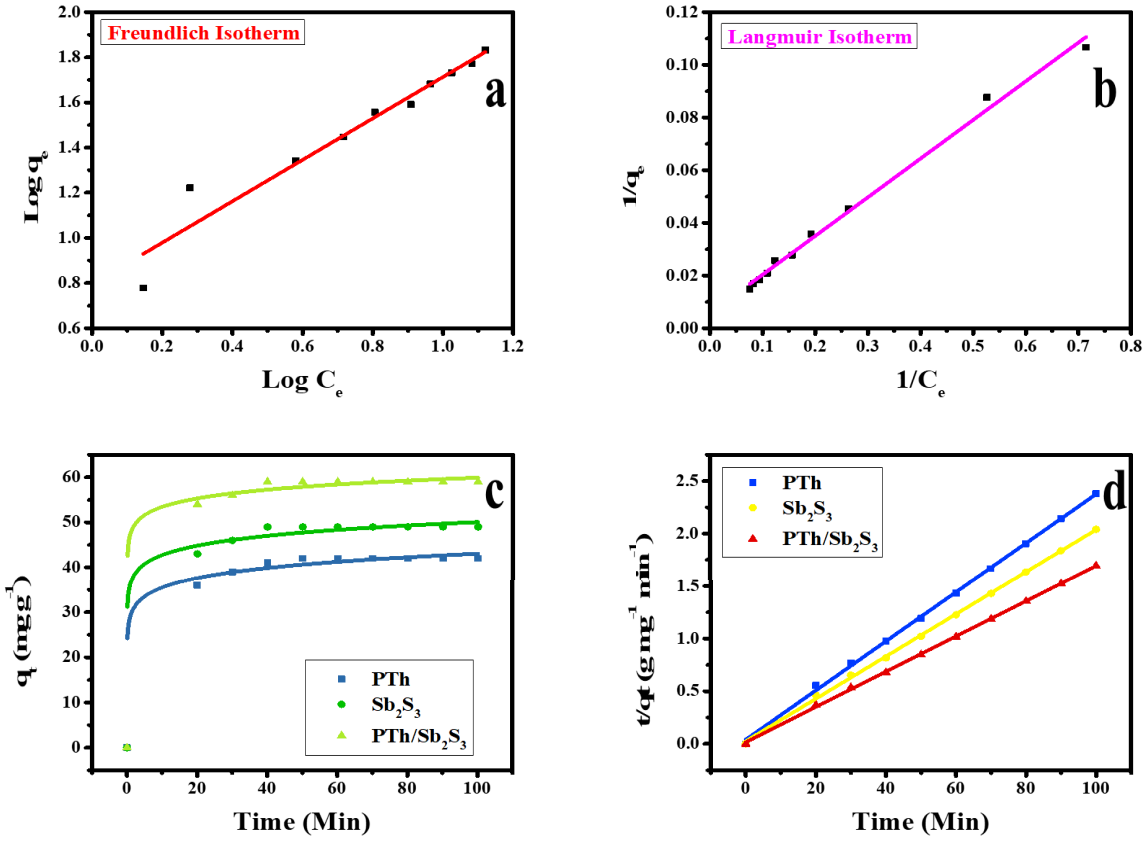

318

319 **Fig.7.** (a) Langmuir isotherm and (b) Freundich adsorption isotherm of PTh/Sb_2S_3 (c) is the
320 pseudo first order and (d) pseudo second order kinetics

321 The fitting of pseudo-second and first order and the rate constant obtained from the equations (8,
322 9) are presented in Table.2.

323 **Table 2: A compare study of the parameters of adsorption and diffusion by PTh, Sb_2S_3 and**
324 **PTh/Sb_2S_3 photocatalysts**

Pseudo-second-order kinetics (diffusion)				
Catalysts	**Fitting equation** $\frac{t}{qe} = \frac{1}{K_2\, qe^2} + \frac{1}{qe}$	**Rate constant (K_2) (g mg^{-1} min^{-1})**	**Correlation coefficient R_d^2**	**Standard Deviation**
PTh	$\frac{t}{qe}$ = 0.0093t + 0.0081	0.0092	0.96	0.11

Sb_2S_3	$\frac{t}{qe}$ = 0.0369t + 0.0581	0.0181	0.98	0.10
PTh/Sb_2S_3	$\frac{t}{qe}$ = 0.0332t + 0.0539	0.0206	0.994	0.09
Pseudo-first-order kinetics (adsorption)				
Catalysts	**Fitting equation ln (qe-qt) = lnqe- K_1t**	**Rate constant (K_1) (g mg^{-1} min^{-1})**	**Correlation coefficient R_a^2**	**Standard Deviation**
PTh	=3.713-(-0.1512)t	0.15	0.74	2.23
Sb_2S_3	=3.657-(-0.1452)t	0.14	0.76	1.81
PTh/Sb_2S_3	=3.502-(-0.1389)t	0.13	0.76	2.23

The correlation coefficient for PTh/Sb_2S_3 (R_d^2 = 0.99 and R_a^2 = 0.76) shows that the adsorption kinetics monitored pseudo first order as well as second order kinetics which indicate that the adsorption takes place followed by diffusion of RhB molecule on the surface of photocatalysts.

4. Conclusions

To conclude, the heterojunction PTh/Sb_2S_3 was found very effective against the removal of RhB dye through adsorption. The catalyst followed both Freundlich and Langmuir isotherm model. The maximum adsorption capacity is found to be 99.8 (mg g^{-1}) when PTh/Sb_2S_3 was applied against RhB dye. The initial concentration was 20 ppm and the equilibrium concentration of 9.2ppm in 100 mins, however when 5ppm concentration was tested the equilibrium concentration was less than 1ppm which is saturation concentration for the removal of dyes. Further, the photocatalyst shows higher correlation coefficient R^2 = 0.9983 which indicate that the photocatalyst followed pseudo second order kinetics model in comparison to pseudo first order kinetics (R^2 = 0.76). Moreover, the catalysts shows sensing nature towards methanol of concentration ranging from 0.1mM to 0.7 mM. The oxidation peaks at 0.4792V shows the sensing of methanol. Therefore it can be concluded that the synthesized catalysts with their excellent adsorption property and surface area, can be applying for the sensing of toxic solvents as well as for the removal of micropollutants from the wastewater.

Acknowledgements

Nafees Ahmad is thankful to the Department of Chemistry, Integral University, Lucknow India, and the Central Instrumentation Facility (CIF) Integral University for providing necessary research facilities. Prof. Masoom Raza Siddiqui and Dr. Saikh Mohammad Wabaidur are grateful to the Researchers Supporting Project Number (RSP2024R326), King Saud University, Riyadh, Saudi Arabia.

Declaration of Conflict of Interest

On the behalf of all the authors, corresponding author declare no conflicts of interest.

References

1. Bolisetty, S., Peydayesh, M., Mezzenga, R. (2019). Sustainable technologies for water purification from heavy metals: review and analysis. Chemical Society Reviews, 48(2), 463-487.
2. Kümmerer, K., Dionysiou, D. D., Olsson, O., Fatta-Kassinos, D. (2019). Reducing aquatic micropollutants–Increasing the focus on input prevention and integrated emission management. Science of the Total Environment, 652, 836-850.
3. Ahmad, N., Anae, J., Khan, M. Z., Sabir, S., Yang, X. J., Thakur, V. K., Coulon, F. (2021). Visible light-conducting polymer nanocomposites as efficient photocatalysts for the treatment of organic pollutants in wastewater. Journal of Environmental Management, 295, 113362.
4. Routoula, E., Patwardhan, S. V. (2020). Degradation of anthraquinone dyes from effluents: a review focusing on enzymatic dye degradation with industrial potential. Environmental science & technology, 54(2), 647-664.
5. Katheresan, V., Kansedo, J., Lau, S. Y. (2018). Efficiency of various recent wastewater dye removal methods: A review. Journal of environmental chemical engineering, 6(4), 4676-4697.
6. Al-Tohamy, R., Ali, S. S., Li, F., Okasha, K. M., Mahmoud, Y. A. G., Elsamahy, T., Sun, J. (2022). A critical review on the treatment of dye-containing wastewater: Ecotoxicological and health concerns of textile dyes and possible remediation approaches for environmental safety. Ecotoxicology and Environmental Safety, 231, 113160.
7. Khan, F. S. A., Mubarak, N. M., Khalid, M., Tan, Y. H., Abdullah, E. C., Rahman, M. E., Karri, R. R. (2021). A comprehensive review on micropollutants removal using carbon nanotubes-based adsorbents and membranes. Journal of Environmental Chemical Engineering, 9(6), 106647.
8. Ahmad, N., Bano, D., Jabeen, S., Ahmad, N., Iqbal, A., Anwer, A. H., Jeong, C. (2023). Insight into the adsorption thermodynamics, kinetics, and photocatalytic studies of

polyaniline/SnS_2 nanocomposite for dye removal. Journal of Hazardous Materials Advances, 10, 100321.
9. Nure, J. F., Nkambule, T. T. (2023). The recent advances in adsorption and membrane separation and their hybrid technologies for micropollutants removal from wastewater. Journal of Industrial and Engineering Chemistry.
10. Liang, J., Liang, K. (2023). Nanobiohybrids: Synthesis strategies and environmental applications from micropollutants sensing and removal to global warming mitigation. Environmental Research, 116317.
11. Saleh, T. A., Fadillah, G., Saputra, O. A. (2019). Nanoparticles as components of electrochemical sensing platforms for the detection of petroleum pollutants: A review. TrAC Trends in Analytical Chemistry, 118, 194-206.
12. Molla, A., Li, Y., Mandal, B., Kang, S. G., Hur, S. H., Chung, J. S. (2019). Selective adsorption of organic dyes on graphene oxide: Theoretical and experimental analysis. Applied Surface Science, 464, 170-177.
13. Luo, Y., Guo, W., Ngo, H. H., Nghiem, L. D., Hai, F. I., Zhang, J., Wang, X. C. (2014). A review on the occurrence of micropollutants in the aquatic environment and their fate and removal during wastewater treatment. Science of the total environment, 473, 619-641.
14. Iqbal, A., Ahamad, T., Qais, F. A., Ahmad, N., Shafi, A., Ahmed, A. S., Srivastava, S. (2023). Proficient visible-light-driven photocatalytic and anti-biofilm activity of biosynthesized CeO_2-graphene oxide nanocomposites. Materials Chemistry and Physics, 298, 127397.
15. Bano, S., Ahmad, N., Sultana, S., Sabir, S., Khan, M. Z. (2019). Preparation and study of ternary polypyrrole-tin oxide-chitin nanocomposites and their potential applications in visible light photocatalysis and sensors. Journal of Environmental Chemical Engineering, 7(2), 103012.
16. Ahmad, N., Sultana, S., Azam, A., Sabir, S., Khan, M. Z. (2017). Novel bio-nanocomposite materials for enhanced biodegradability and photocatalytic activity. New Journal of Chemistry, 41(18), 10198-10207.
17. Uddin, M. J., Ampiaw, R. E., Lee, W. (2021). Adsorptive removal of dyes from wastewater using a metal-organic framework: A review. Chemosphere, 284, 131314.
18. Zhang, Y., Chen, Z., Shi, Z., Lu, T. T., Chen, D., Wang, Q., Zhan, Z. (2021). A direct Z-scheme BiOBr/TzDa COF heterojunction photocatalyst with enhanced performance on visible-light driven removal of organic dye and Cr (VI). Separation and Purification Technology, 275, 119216.
19. Iqbal, A., Ahmed, A. S., Ahmad, N., Shafi, A., Ahamad, T., Khan, M. Z., Srivastava, S. (2021). Biogenic synthesis of CeO_2 nanoparticles and its potential application as an efficient photocatalyst for the degradation of toxic amido black dye. Environmental Nanotechnology, Monitoring & Management, 16, 100505.
20. Ayappan, C., Jayaraman, V., Palanivel, B., Pandikumar, A., Mani, A. (2020). Facile preparation of novel Sb_2S_3 nanoparticles/rod-like α-Ag_2WO_4 heterojunction

photocatalysts: continuous modulation of band structure towards the efficient removal of organic contaminants. Separation and Purification Technology, 236, 116302.

21. Xiao, Y., Wang, H., Jiang, Y., Zhang, W., Zhang, J., Wu, X., Deng, W. (2022). Hierarchical $Sb_2S_3/ZnIn_2S_4$ core–shell heterostructure for highly efficient photocatalytic hydrogen production and pollutant degradation. Journal of Colloid and Interface Science, 623, 109-123.
22. Karimi-Shamsabadi, M., Behpour, M. (2021). Comparing photocatalytic activity consisting of Sb_2S_3 and Ag_2S on the $TiO_2–SiO_2/TiO_2$ nanotube arrays-support for improved visible-light-induced photocatalytic degradation of a binary mixture of basic blue 41 and basic red 46 dyes. International Journal of Hydrogen Energy, 46(53), 26989-27013.
23. Wang, H., Yuan, X., Wang, H., Chen, X., Wu, Z., Jiang, L., Zeng, G. (2016). Facile synthesis of Sb_2S_3/ultrathin g-C_3N_4 sheets heterostructures embedded with g-C_3N_4 quantum dots with enhanced NIR-light photocatalytic performance. Applied Catalysis B: Environmental, 193, 36-46.
24. Faisal, M., Harraz, F. A., Ismail, A. A., El-Toni, A. M., Al-Sayari, S. A., Al-Hajry, A., Al-Assiri, M. S. (2018). Polythiophene/mesoporous $SrTiO_3$ nanocomposites with enhanced photocatalytic activity under visible light. Separation and Purification Technology, 190, 33-44.
25. Hadia, N. M. A., Mohamed, W. S., Abd El-sadek, M. S. (2019). Simultaneous synthesis of various Sb_2S_3 nanostructures by vapor transport technique. Materials Chemistry and Physics, 235, 121750.
26. Kalangestani, F. C., Ghodsi, F. E., & Bazhan, Z. (2020). Investigating the effect of Zn doping on physical properties of nanostructured Sb_2S_3 thin films by dip-coating technique. Applied Physics A, 126, 1-8.
27. Trivedi, M., Nayak, G., Patil, S., Tallapragada, R. M., Latiyal, O. (2015). Impact of biofield treatment on physical, structural and spectral properties of antimony sulfide. Industrial Engineering & Management, 4(3), 1000165.
28. Dashairya, L., Sharma, M., Basu, S., Saha, P. (2018). Enhanced dye degradation using hydrothermally synthesized nanostructured Sb_2S_3/rGO under visible light irradiation. Journal of Alloys and Compounds, 735, 234-245.
29. Subramanian, S., Padiyan, D. P. (2010). Enhanced electrical response in Sb_2S_3 thin films by the inclusion of polyaniline during electrodeposition. Physica B: Condensed Matter, 405(3), 925-931.
30. Hou, W., Guo, H., Zhang, J., Xu, J., Liu, L., Zhang, Z., Zhang, H. (2018). Facile synthesis and hydrazine detection activity of Sb2S3 films on indium tin oxide electrode. Materials Letters, 216, 73-76.
31. Tezel, N. S., Tezel, F. M., Kariper, İ. A. (2019). Surface and electro-optical properties of amorphous Sb_2S_3 thin films. Applied Physics A, 125, 1-16.

32. Xiao, K., Xu, Q. Z., Ye, K. H., Liu, Z. Q., Fu, L. M., Li, N., Su, Y. Z. (2013). Facile hydrothermal synthesis of Sb_2S_3 nanorods and their magnetic and electrochemical properties. ECS Solid State Letters, 2(6), P51.
33. Hassanian-Moghaddam, H., Rafizadeh, A., Shariati, S., Rafizadeh, M., Zamani, N. (2018). Evaluation of methanol content of beverages using an easy modified chromotropic acid method. Food and chemical toxicology, 121, 11-14.
34. Wang, G., Morrin, A., Li, M., Liu, N., Luo, X. (2018). Nanomaterial-doped conducting polymers for electrochemical sensors and biosensors. Journal of Materials Chemistry B, 6(25), 4173-4190.
35. Ahmad, N., Sultana, S., Faisal, S. M., Ahmed, A., Sabir, S., Khan, M. Z. (2019). Zinc oxide-decorated polypyrrole/chitosan bionanocomposites with enhanced photocatalytic, antibacterial and anticancer performance. RSC advances, 9(70), 41135-41150.
36. Chung, D. Y., Lee, K. J., Sung, Y. E. (2016). Methanol electro-oxidation on the Pt surface: revisiting the cyclic voltammetry interpretation. The Journal of Physical Chemistry C, 120(17), 9028-9035.
37. Kusmierek, K., Fronczyk, J., Swiątkowski, A. (2023). Adsorptive removal of rhodamine B dye from aqueous solutions using mineral materials as low-cost adsorbents. Water, Air, & Soil Pollution, 234(8), 531.
38. Kumar, V. (2019). Adsorption kinetics and isotherms for the removal of rhodamine B dye and Pb^{+2} ions from aqueous solutions by a hybrid ion-exchanger. Arabian Journal of Chemistry, 12(3), 316-329